Utilizing complex oxide substrates to control carrier concentration in large-area monolayer MoS$_2$ films

Xudong Zheng, Eli Gerber, (iD) Jisung Park, et al.

View Online   Export Citation   CrossMark

ARTICLES YOU MAY BE INTERESTED IN

Utilizing complex oxide substrates to control carrier concentration in large-area monolayer MoS₂ films

View Online   Export Citation   CrossMark

Xudong Zheng,[1] Eli Gerber,[2] Jisung Park,[1] (iD) Don Werder,[1,3] Orrin Kigner,[1] Eun-Ah Kim,[4] Saien Xie,[1,4,5,a] (iD)
and Darrell G. Schlom[1,5,6,a] (iD)

AFFILIATIONS

[1]Department of Materials Science and Engineering, Cornell University, Ithaca, New York 14853, USA
[2]School of Applied and Engineering Physics, Cornell University, Ithaca, New York 14853, USA
[3]Platform for the Accelerated Realization, Analysis, and Discovery of Interface Materials (PARADIM), Cornell University, Ithaca, New York 14853, USA
[4]Department of Physics, Laboratory of Atomic and Solid State Physics, Cornell University, Ithaca, New York 14853, USA
[5]Kavli Institute at Cornell for Nanoscale Science, Ithaca, New York 14853, USA
[6]Leibniz-Institut für Kristallzüchtung, Max-Born-Str.. 2, 12489 Berlin, Germany

[a]Authors to whom correspondence should be addressed: sx68@cornell.edu and schlom@cornell.edu

ABSTRACT

Bandgap engineering is central to the design of heterojunction devices. For heterojunctions involving monolayer-thick materials like MoS₂, the carrier concentration of the atomically thin film can vary significantly depending on the amount of charge transfer between MoS₂ and the substrate. This makes substrates with a range of charge neutrality levels—as is the case for complex oxide substrates—a powerful addition to electrostatic gating or chemical doping to control the doping of overlying MoS₂ layers. We demonstrate this approach by growing monolayer MoS₂ on perovskite (SrTiO₃ and LaAlO₃), spinel (MgAl₂O₄), and SiO₂ substrates with multi-inch uniformity. The as-grown MoS₂ films on these substrates exhibit a controlled, reproducible, and uniform carrier concentration ranging from $(1-4) \times 10^{13}$ cm^{-2}, depending on the oxide substrate employed. The observed carrier concentrations are further confirmed by our density-functional theory calculations based on *ab initio* mismatched interface theory (MINT). This approach is relevant to large-scale heterostructures involving monolayer-thick materials in which it is desired to precisely control carrier concentrations for applications.

Published under license by AIP Publishing. https://doi.org/10.1063/5.0038383

Interfaces between dissimilar materials have enabled a variety of key technologies[1] including high-efficiency light-emitting diodes,[2] solar cells,[3,4] and quantum electronics.[5] Two-dimensional transition metal dichalcogenides (TMDs), with a wide range of band structures and direct bandgaps at monolayer thicknesses, provide a unique material platform for interface-engineered electronics.[6] Due to their atomic thinness, the electronic properties of monolayer TMDs can be widely tuned by the substrate. For instance, monolayer molybdenum disulfide (MoS₂), one of the most studied TMDs, exhibits a higher electron concentration on SiO₂ substrates than when prepared on SrTiO₃, h-BN, or Gel-Film®.[7–9] Understanding and further controlling the substrate-dependent carrier concentration are, thus, important for developing TMD-based electronics.

Unlike three-dimensional semiconductor heterostructures, the atomic thinness of monolayer TMDs (< 1 nm) limits the formation of a depletion or accumulation region.[10] As a result, the difference between the charge neutrality level of a TMD and the underlying substrate leads to a change in the carrier concentration of TMDs through a charge transfer process to ensure an aligned Fermi level.[7,11] This enables direct control of the carrier concentration in monolayer TMDs by selecting different substrates. Complex oxides, with a range of charge neutrality levels, provide a means for tuning the carrier concentration in TMDs that can supplement electrostatic gating or chemical doping,[12–14] which are crucial for device applications (e.g., *p–n* junctions and transistors). For example, a complex oxide substrate can be used to uniformly shift the threshold voltage in a TMD-based transistor. The atomically smooth surface of complex oxide substrates further promotes the formation of a high-quality interface to TMDs with minimal charged impurities.[15]

Although charge transfer has been widely studied between graphene and oxide substrates,[16–19] semiconducting TMDs have been

synthesized mainly on SiO_2,[20–22] and interfacing TMDs with functional complex oxides remains a largely untapped avenue for altering the electronic properties of the TMDs. While exfoliated MoS_2 on $LaAlO_3$ and $SrTiO_3$ has been shown to have different carrier concentrations,[7] large-scale growth of MoS_2 on complex oxide substrates with a controlled carrier concentration remains an unsolved challenge, as existing solid-precursor-based CVD only produces monolayer MoS_2 with limited spatial uniformity.[23–25]

Here, we report the large-scale growth of monolayer MoS_2 with reproducible and controlled carrier concentrations on a series of complex oxides including perovskites ($SrTiO_3$ and $LaAlO_3$) and spinel

($MgAl_2O_4$). This monolayer MoS_2 is synthesized on complex oxides with spatial uniformity across three inches, taking advantage of a metal-organic chemical vapor deposition (MOCVD) method that uses precisely controlled gas-phase precursors to improve uniformity.[26] The electron concentrations of MoS_2 on complex oxides are substrate dependent and are all lower than those of MoS_2 on SiO_2, as revealed by our Raman and photoluminescence spectroscopy (PL) measurements. The Raman and PL measurements are all performed at room temperature. To understand the observed substrate-dependent electron concentration of MoS_2, we performed density-functional theory (DFT) calculations using *ab initio* mismatched interface theory
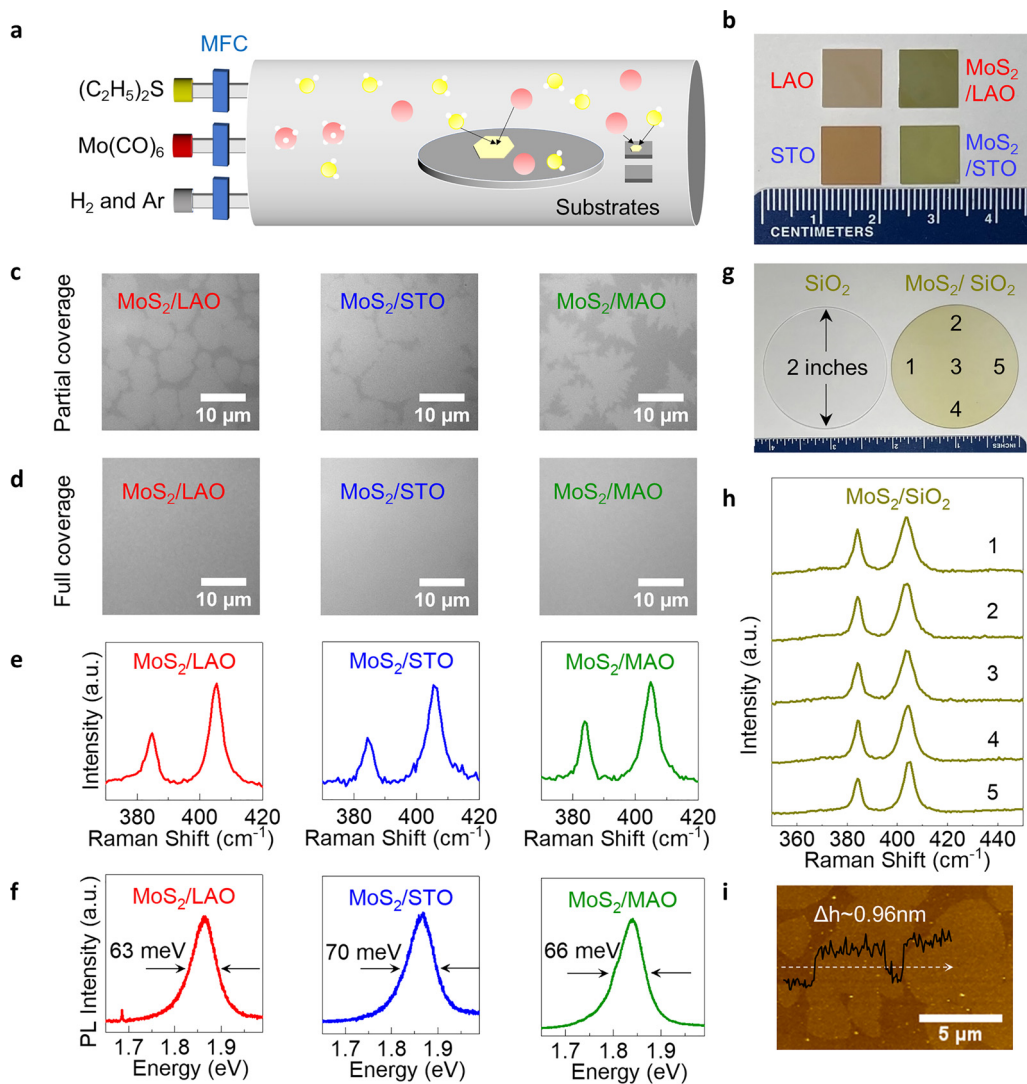
FIG. 1. Uniform growth of monolayer-thick MoS_2 on (100) $LaAlO_3$, (100) $SrTiO_3$, (100) $MgAl_2O_4$, and amorphous SiO_2. (a) Schematic of the MOCVD growth process. Precursors are independently introduced into the furnace. Yellow, sulfur atom; red, molybdenum atom; white, carbonyl or ethyl ligand. (b) Photograph of monolayer MoS_2 grown on $1 \times 1\,cm^2$ $LaAlO_3$ and $SrTiO_3$ substrates. Bare substrates are shown on the left for comparison. (c) Optical micrographs of monolayer MoS_2 with partial coverage and (d) full coverage on $LaAlO_3$, $SrTiO_3$, and $MgAl_2O_4$, respectively. (e) Raman and (f) photoluminescence spectra of MoS_2 on $LaAlO_3$, $SrTiO_3$, and $MgAl_2O_4$. (g) Photograph of monolayer MoS_2 grown on a 2 in. diameter fused silica substrate. A bare substrate is shown on the left for comparison. (h) Raman spectra for MoS_2 taken at different locations marked on the corresponding fused silica wafer from (g). (i) AFM image of monolayer MoS_2 grown on $LaAlO_3$.

(MINT),[27] and the calculated magnitudes of electron transfer showed excellent agreement with our observations. In comparison, it has been challenging to treat these heterostructures using previous DFT methods, as they are often incommensurate due to the distinct lattice symmetry and large lattice mismatch.

Figure 1 shows uniform, monolayer MoS_2 films deposited on (100) $SrTiO_3$, (100) $LaAlO_3$, (100) $MgAl_2O_4$ (denoted as STO, LAO, and MAO, respectively), and amorphous SiO_2 substrates. The growth was carried out in a home-built MOCVD system following the design of Kang et al. [Fig. 1(a)], using gas-phase precursors of $Mo(CO)_6$ and $(C_2H_5)_2S$ (see the experimental methods in the supplementary material for details).[26] The as-grown films are homogenously yellow in appearance and are clearly distinguishable from the bare substrates [Figs. 1(b) and 1(g)]. We assessed the quality of the as-grown monolayer MoS_2 using optical imaging, Raman, PL, and atomic force microscopy (AFM). Figures 1(c) and 1(d) show the optical micrographs of MoS_2 with partial coverage and full coverage, where no multilayer region was observed before the completion of the growth of the first layer. Raman spectroscopy reveals characteristic E_{2g}^1 and A_{1g} peaks of MoS_2 at 384.1 and 403.6 cm^{-1} for MoS_2/SiO_2 [Fig. 1(h)], 384.4 and 405.2 cm^{-1} for $MoS_2/LaAlO_3$, 384.5 and 405.6 cm^{-1} for $MoS_2/SrTiO_3$, and 383.8 and 404.9 cm^{-1} for $MoS_2/MgAl_2O_4$, respectively [Fig. 1(e)] (see Fig. S1 in the supplementary material for background subtraction), suggesting the high structural quality of our monolayer MoS_2.[7,28] The PL spectra show a sharp A exciton peak for $MoS_2/LaAlO_3$ and $MoS_2/SrTiO_3$ (centered at 1.86 eV), as well as for $MoS_2/MgAl_2O_4$ (centered at 1.84 eV) [Fig. 1(f)], consistent with a previous report on an exfoliated sample.[7] The full width at half maximum (FWHM) of the PL peaks on all substrates was smaller than 70 meV. An AFM image of monolayer MoS_2 grown on $LaAlO_3$ shows a thickness of 0.96 nm [Fig. 1(i)], confirming the monolayer thickness.[29] Taken together, these features confirm the high quality of the monolayer MoS_2 grown on these oxide substrates.

The large-scale uniformity of MoS_2 on complex oxides is verified by the identical growth behavior observed on substrates placed 8 cm apart in the MOCVD furnace and further corroborated by the uniform growth of MoS_2 on a 2 in. SiO_2 wafer. MoS_2 grown on complex oxide substrates placed 8 cm apart shows the same grain size, nucleation density (Fig. S2), Raman features [Fig. 2(c)], and PL spectra [Fig. 3(f)]. The as-grown MoS_2 on a 2 in. fused silica wafer [Fig. 1(f)] shows a homogeneous, greenish-yellow color. Optical micrographs (Fig. S3) and Raman spectra [Fig. 1(h)] taken at different locations across the wafer, as marked in Fig. 1(g), show identical features, confirming the wafer-scale uniformity of MoS_2 grown.

A semiconductor-insulator junction forms when MoS_2 is grown on the above substrates. This leads to charge transfer to preserve alignment of the Fermi level.[11] Using Raman and PL spectroscopies, we demonstrate that the carrier concentration of MoS_2 can be controlled by the substrate upon which it is grown. Figure 2(a) compares the Raman spectra of MoS_2 grown on SiO_2, $MgAl_2O_4$, $LaAlO_3$, and $SrTiO_3$. The E_{2g}^1 mode (in-plane vibration) shows little dependence on the substrate. Specifically, only small shifts in the E_{2g}^1 peak position of -0.26 cm^{-1} for $MoS_2/MgAl_2O_4$, $+0.38$ cm^{-1} for $MoS_2/LaAlO_3$, and $+0.44$ cm^{-1} for $MoS_2/SrTiO_3$ are observed relative to those of MoS_2/SiO_2 [Fig. 2(b)]. The E_{2g}^1 peak position is known to depend linearly on the magnitude of the strain.[30,31] From previous studies, E_{2g}^1 peak shifts by 2.1 cm^{-1} per % of uniaxial strain[30] and by 5.2 cm^{-1} per % of biaxial strain.[31] Thus, the strain in our MoS_2 films on complex oxides does not exceed 0.21% (uniaxial) or 0.09% (biaxial). The minimal magnitude of strain suggests that the intrinsic lattice constant of MoS_2 is not being perturbed by the underlying substrate.

In contrast to the E_{2g}^1 peak, the A_{1g} peak exhibits a sizeable blue shift as well as a narrower FWHM [Fig. 2(b)], when the substrate is changed from SiO_2 to complex oxides. The blue shift is uniform across the entire film, as seen by the narrow distribution of the A_{1g} peak position measured at ten locations on two substrates placed 8 cm apart during growth [Figs. 2(c) and S2]. The distributions of the A_{1g} peak position display blue shifts of 1.28 ± 0.04 cm^{-1} (for $MgAl_2O_4$), 1.66 ± 0.06 cm^{-1} (for $LaAlO_3$), and 1.98 ± 0.06 cm^{-1} (for $SrTiO_3$) relative to MoS_2 grown on SiO_2. The position of the A_{1g} peak is sensitive
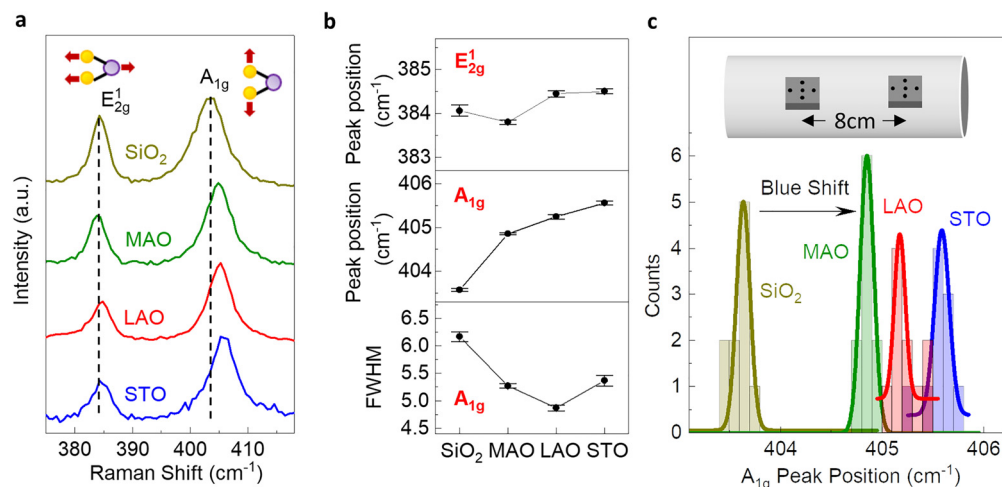
FIG. 2. Raman of monolayer MoS_2 deposited on SiO_2, $MgAl_2O_4$, $LaAlO_3$, and $SrTiO_3$ substrates. (a) Normalized Raman spectra of monolayer MoS_2. (b) From top to bottom: dependence of the E_{2g}^1 peak position, A_{1g} peak position, and FWHM of the A_{1g} peak on substrates indicated. (c) Histograms and their Gaussian fittings of the A_{1g} peak position of MoS_2 on different substrates. Ten measurements were taken from two substrates placed 8 cm apart (inset) for each type of substrate.

to strain[30,31] and to electron doping due to the much stronger electron-phonon coupling of the A_{1g} mode compared to the E_{2g}^1 mode.[32] Since the Raman measurements show the strain effect to be minimal, we attribute these sizable blue shifts in the A_{1g} peak to different amounts of charge transferred from the substrates. Based on the reported relationship between the electron density and the A_{1g} peak position,[32] the electron densities of monolayer MoS_2 grown on $MgAl_2O_4$, $LaAlO_3$, and $SrTiO_3$ are estimated to be $0.30 \times 10^{13}\,cm^{-2}$, $0.48 \times 10^{13}\,cm^{-2}$, and $0.65 \times 10^{13}\,cm^{-2}$ lower than when MoS_2 is deposited on SiO_2, respectively.

The difference in electron density for MoS_2 grown on different substrates is further confirmed by PL spectroscopy. As a direct bandgap semiconductor, MoS_2 shows strong PL emission at room temperature,[33] and the prominent A exciton peak can evolve into multiple peaks corresponding to a neutral exciton (A^0), a negatively charged trion consisting of two electrons and one hole (A^-),[12] or a positively charged trion consisting of one electron and two holes (A^+) [Fig. 3(a)].[13] For n-doped MoS_2, the intensity ratio of negatively charged trions and neutral excitons can be used to determine the corresponding electron concentration.[14]

Figure 3(b) presents the PL spectra for monolayer MoS_2 on SiO_2, $MgAl_2O_4$, $LaAlO_3$, and $SrTiO_3$, together with three Lorentzian functions fitted to peaks corresponding to A^- (red curve), A^0 (blue curve), and B (gray curve) excitons.[33] We note that the A^- and A^0 peaks show blue shifts when the substrate is varied from SiO_2 to $MgAl_2O_4$, $LaAlO_3$, and $SrTiO_3$. This is caused by the dielectric screening of the

Coulomb interactions.[34] As the dielectric constant increases from SiO_2 ($\kappa \approx 4$) to $MgAl_2O_4$ ($\kappa \approx 8$), $LaAlO_3$ ($\kappa \approx 24$), and $SrTiO_3$ ($\kappa \approx 300$),[35–37] both the electronic bandgap and the exciton binding energies of MoS_2 decrease, leading to a small blue shift of A^- and A^0 PL peaks. We note that the large κ of $SrTiO_3$ does not result in a substantial blue shift, which is caused by the PL peak energy approaching the electronic bandgap. This observation is consistent with previous report by Lin et $al.$[34] that A^- and A^0 peak positions start to saturate (approaching the electronic bandgap) as the relative dielectric constant of the environment exceeds 18.

Figure 3(d) compares the intensity ratio between the trion peak and the neutral exciton peak (I_{A^-}/I_{A^0}). MoS_2/SiO_2 has the highest I_{A^-}/I_{A^0} intensity ratio of 1.62 ± 0.12, while this value drastically decreases to 0.60 ± 0.03 for $MoS_2/MgAl_2O_4$, 0.52 ± 0.03 for $MoS_2/LaAlO_3$, and 0.46 ± 0.06 for $MoS_2/SrTiO_3$. Based on the quantitative relation from the mass-action model, which estimates the exciton and trion population by assuming dynamic equilibrium ($A^0 + e^- \leftrightarrow A^-$),[14] the differences in the electron concentration are estimated to be Δn (MoS_2/SiO_2 - $MoS_2/MgAl_2O_4$) $\approx 2.53 \times 10^{13}\,cm^{-2}$, Δn ($MoS_2/SiO_2 - MoS_2/LaAlO_3$) $\approx 2.70 \times 10^{13}\,cm^{-2}$, and Δn ($MoS_2/SiO_2 - MoS_2/SrTiO_3$) $\approx 2.89 \times 10^{13}\,cm^{-2}$ [Fig. 3(e)]. The lower, and closer to intrinsic, electron density of MoS_2 on complex oxides than on SiO_2 might be enabled by the atomically smooth surfaces of complex oxide substrates with reduced interfacial impurities.[8,15,38] The large-scale uniformity of the electron concentration in our MoS_2 films is corroborated by the narrow distributions in the histogram of the trion spectral weight
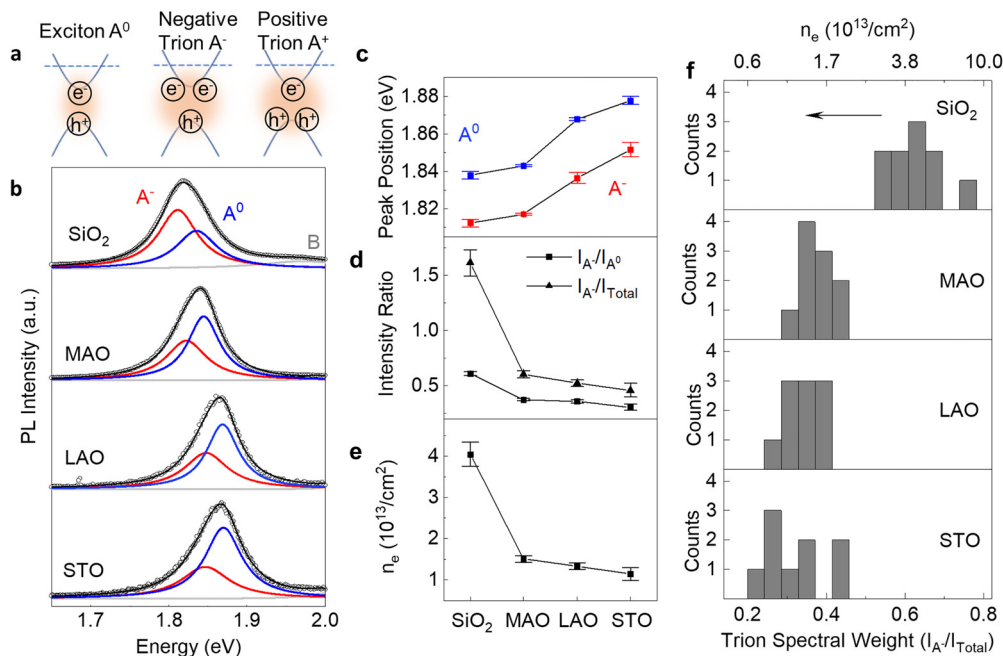
FIG. 3. Effect of the substrate on the photoluminescence of monolayer MoS_2. (a) Schematics of the neutral exciton (A^0), negative trion (A^-), and positive trion (A^+). (b) PL of monolayer MoS_2 grown on different substrates. (c) Peak position of A^0 and A^- as a function of substrate materials. (d) The intensity ratio between negative trion emission and neutral exciton emission (I_{A^-}/I_{A^0}) and between negative trion emission and total A exciton emission (I_{A^-}/I_{Total}), in which $I_{Total} = I_{A^-} + I_{A^0}$. (e) Estimated electron density in MoS_2 as a function of substrate material. (f) Histograms of trion spectral weight (I_{A^-}/I_{Total}) of MoS_2 on different substrates. For each substrate, ten different measurements were taken from two substrates placed 8 cm apart during growth, as shown in [Fig. 2(c)]. The top axis shows the corresponding electron density calculated from a mass action model.[14]

[Fig. 3(f)] calculated from PL spectra measured at different locations on two substrates placed 8 cm apart during growth.

The observed changes in the Raman A_{1g} peak frequency and the trion-to-neutral-exciton intensity ratio show a consistent trend of electron transfer variation among MoS_2 on different substrates [Fig. 4(a)]. In particular, MoS_2 grown on SiO_2 has a much higher electron concentration than does MoS_2 grown on complex oxides; MoS_2 grown on $MgAl_2O_4$, $LaAlO_3$, and $SrTiO_3$ shows a progressive decrease in the electron concentration. We note that the electron concentrations estimated by PL using the mass action model[14] are significantly higher than those derived from the Raman peak shift measured in a MoS_2-based field-effect transistor.[32] These differences could be due to several reasons. For instance, the defect levels of our films can be different from exfoliated MoS_2 devices studied in previous reports, which can lead to different Raman responses. While the carrier concentration of the MoS_2 film can, in principle, be directly measured utilizing the Hall effect, the low conductivity of the as-grown film makes such Hall measurements challenging.

To understand the observed substrate-induced charge transfer, we performed *ab initio* mismatched interface theory[27] (MINT) calculations of increasingly large MoS_2 clusters (3, 6, 12, and 18 unit cells, respectively, see Fig. S4 in the supplementary material) above each oxide substrate layer. The finite-size scaling of the cluster calculations predicts electron concentrations of 2.49 ± 0.89, 1.38 ± 0.18, 1.15 ± 0.09, and 0.97 ± 0.19 (in units of $10^{13}\,cm^{-2}$) for MoS_2 on SiO_2, $MgAl_2O_4$, $LaAlO_3$, and $SrTiO_3$, respectively. These results are in good agreement with the carrier concentrations derived from PL measurements [Fig. 4(b)]. Specifically, the MINT predicted values for MoS_2 on complex oxides are very close to those derived from PL ($<15\%$ lower). For MoS_2 on SiO_2, the difference between MINT and PL is larger ($\sim38\%$ lower). This underestimation of the carrier concentration can likely be attributed to carriers released from depopulated trap states at the interface of MoS_2/SiO_2, which are not considered in MINT calculations and could, thus, result in higher doping.[39] On the other hand, such interfacial impurities of MoS_2 on complex oxides could be much less than on SiO_2 due to the well defined nature of their crystalline and atomically smooth surfaces.

In conclusion, monolayer MoS_2 was grown on spinel ($MgAl_2O_4$) and perovskite ($SrTiO_3$ and $LaAlO_3$) substrates by MOCVD with 3 in. uniformity. Our Raman and PL measurements combined with

ab initio calculations (MINT) establish that MoS_2 grown on these substrates exhibits a controlled, reproducible, and uniform carrier concentration depending on the oxide substrate employed. This large-scale MOCVD process at relatively low growth temperature is not limited to MoS_2 on $MgAl_2O_4$, $LaAlO_3$, and $SrTiO_3$. It can be readily applied to create interfaces between semiconducting TMDs and a myriad of complex oxides. Indeed, our preliminary attempts show that MoS_2 growths are also possible on gadolinium gallium garnet (GGG), $YAlO_3$, and sapphire (Fig. S5 in the supplementary material). Our results demonstrate a means to provide uniform and reproducible electron transfer over large areas. Thus, complex oxide substrates possess significant potential for creating wafer-scale TMD-based devices with various electronic and optoelectronic properties.

See the supplementary material for experimental methods, detailed optical characterization of MoS_2/oxides, MINT calculations, growth results on more complex oxides, fast growth of MoS_2 on SiO_2, and charge transfer between MoS_2 and Nb-doped $SrTiO_3$.
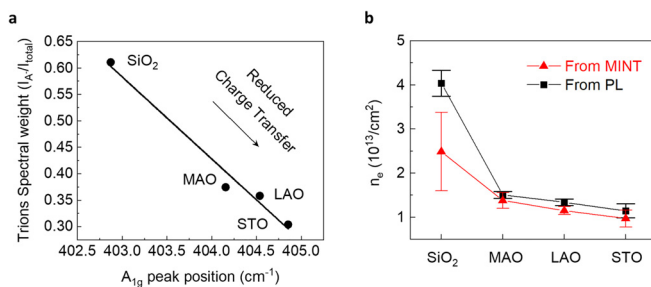
DATA AVAILABILITY

The data supporting the findings of this study are available within the paper. Additional data related to the growth and structural characterization are available at https://doi.org/10.34863/083j-x818. Any additional data connected to the study are available from the corresponding author upon reasonable request.

FIG. 4. Charge transfer between substrates and MoS_2. (a) The trion spectral weight $[I_{A^-}/(I_{A^-} + I_{A^0})]$ as a function of the corresponding A_{1g} peak position for MoS_2 grown on different substrates and its linear fit. The top-left of the diagram corresponds to high electron transfer from the substrate to MoS_2 and the bottom-right corner to low electron transfer from the substrate to MoS_2. (b) Comparison of the electron concentration of MoS_2 on different oxide substrates made between calculated values based on MINT and measurements based on PL.

REFERENCES

[1]H. Kroemer, Rev. Mod. Phys. **73**, 783 (2001).
[2]Y. Yang, Y. Zheng, W. Cao, A. Titov, J. Hyvonen, J. R. Manders, J. Xue, P. H. Holloway, and L. Qian, Nat. Photonics **9**, 259 (2015).
[3]B. O'Regan and M. Grätzel, Nature **353**, 737 (1991).
[4]M. M. Lee, J. Teuscher, T. Miyasaka, T. N. Murakami, and H. J. Snaith, Science **338**, 643 (2012).
[5]F. A. Zwanenburg, A. S. Dzurak, A. Morello, M. Y. Simmons, L. C. Hollenberg, G. Klimeck, S. Rogge, S. N. Coppersmith, and M. A. Eriksson, Rev. Mod. Phys. **85**, 961 (2013).
[6]S. Manzeli, D. Ovchinnikov, D. Pasquier, O. V. Yazyev, and A. Kis, Nat. Rev. Mater. **2**, 17033 (2017).
[7]Y. Li, Z. Qi, M. Liu, Y. Wang, X. Cheng, G. Zhang, and L. Sheng, Nanoscale **6**, 15248 (2014).
[8]M. Buscema, G. A. Steele, H. S. van der Zant, and A. Castellanos-Gomez, Nano Res. **7**, 561 (2014).
[9]W. H. Chae, J. D. Cain, E. D. Hanson, A. A. Murthy, and V. P. Dravid, Appl. Phys. Lett. **111**, 143106 (2017).
[10]D. Pierucci, H. Henck, J. Avila, A. Balan, C. H. Naylor, G. Patriarche, Y. J. Dappe, M. G. Silly, F. Sirotti, A. T. C. Johnson, M. C. Asensio, and A. Ouerghi, Nano Lett. **16**, 4054 (2016).
[11]J. Robertson, J. Vac. Sci. Technol. B **18**, 1785 (2000).

[12]K. F. Mak, K. He, C. Lee, G. H. Lee, J. Hone, T. F. Heinz, and J. Shan, Nat. Mater. **12**, 207 (2013).

[13]J. S. Ross, S. Wu, H. Yu, N. J. Ghimire, A. M. Jones, G. Aivazian, J. Yan, D. G. Mandrus, D. Xiao, W. Yao, and X. Xu, Nat. Commun. **4**, 1 (2013).

[14]S. Mouri, Y. Miyauchi, and K. Matsuda, Nano Lett. **13**, 5944 (2013).

[15]K. T. Kang, J. Park, D. Suh, and W. S. Choi, Adv. Mater. **31**, 1803732 (2019).

[16]P. A. Khomyakov, G. Giovannetti, P. C. Rusu, G. Brocks, J. van den Brink, and P. J. Kelly, Phys. Rev. B **79**, 195425 (2009).

[17]D. Jin, A. Kumar, K. Hung Fung, J. Xu, and N. X. Fang, Appl. Phys. Lett. **102**, 201118 (2013).

[18]P. K. Gogoi, P. E. Trevisanutto, M. Yang, I. Santoso, T. C. Asmara, A. Terentjevs, F. D. Sala, M. B. H. Breese, T. Venkatesan, Y. P. Feng, K. P. Loh, A. H. Castro Neto, and A. Rusydi, Phys. Rev. B **91**, 035424 (2015).

[19]D. Shin and A. A. Demkov, Phys. Rev. B **97**, 075423 (2018).

[20]B. Radisavljevic, A. Radenovic, J. Brivio, V. Giacometti, and A. Kis, Nat. Nanotechnol. **6**, 147 (2011).

[21]Z. Yin, H. Li, H. Li, L. Jiang, Y. Shi, Y. Sun, G. Lu, Q. Zhang, X. Chen, and H. Zhang, ACS Nano **6**, 74 (2012).

[22]K. F. Mak, K. L. McGill, J. Park, and P. L. McEuen, Science **344**, 1489 (2014).

[23]Y. Zhang, Q. Ji, G. F. Han, J. Ju, J. Shi, D. Ma, J. Sun, Y. Zhang, M. Li, X. Y. Lang, Y. Zhang, and Z. Liu, ACS Nano **8**, 8617 (2014).

[24]C. Li, Y. Zhang, Q. Ji, J. Shi, Z. Chen, X. Zhou, Q. Fang, and Y. Zhang, 2D Mater. **3**, 035001 (2016).

[25]P. Chen, W. Xu, Y. Gao, J. H. Warner, and M. R. Castell, ACS Appl. Nano Mater. **1**, 6976 (2018).

[26]K. Kang, S. Xie, L. Huang, Y. Han, P. Y. Huang, K. F. Mak, C. J. Kim, D. Muller, and J. Park, Nature **520**, 656 (2015).

[27]E. Gerber, Y. Yao, T. A. Arias, and E. A. Kim, Phys. Rev. Lett. **124**, 106804 (2020).

[28]H. Li, Q. Zhang, C. C. R. Yap, B. K. Tay, T. H. T. Edwin, A. Olivier, and D. Baillargeat, Adv. Funct. Mater. **22**, 1385 (2012).

[29]Y. H. Lee, X. Q. Zhang, W. Zhang, M. T. Chang, C. Te Lin, K. D. Chang, Y. C. Yu, J. T. W. Wang, C. S. Chang, L. J. Li, and T. W. Lin, Adv. Mater. **24**, 2320 (2012).

[30]C. Rice, R. J. Young, R. Zan, U. Bangert, D. Wolverson, T. Georgiou, R. Jalil, and K. S. Novoselov, Phys. Rev. B **87**, 081307 (2013).

[31]D. Lloyd, X. Liu, J. W. Christopher, L. Cantley, A. Wadehra, B. L. Kim, B. B. Goldberg, A. K. Swan, and J. S. Bunch, Nano Lett. **16**, 5836 (2016).

[32]B. Chakraborty, A. Bera, D. V. S. Muthu, S. Bhowmick, U. V. Waghmare, and A. K. Sood, Phys. Rev. B **85**, 161403 (2012).

[33]K. F. Mak, C. Lee, J. Hone, J. Shan, and T. F. Heinz, Phys. Rev. Lett. **105**, 136805 (2010).

[34]Y. Lin, X. Ling, L. Yu, S. Huang, A. L. Hsu, Y. H. Lee, J. Kong, M. S. Dresselhaus, and T. Palacios, Nano Lett. **14**, 5569 (2014).

[35]L. F. Edge, D. G. Schlom, P. Sivasubramani, R. M. Wallace, B. Holländer, and J. Schubert, Appl. Phys. Lett. **88**, 112907 (2006).

[36]R. D. Shannon and G. R. Rossman, J. Phys. Chem. Solids **52**, 1055 (1991).

[37]B. K. Choudhury, K. V. Rao, and R. N. P. Choudhury, J. Mater. Sci. **24**, 3469 (1989).

[38]M. Kawasaki, K. Takahashi, T. Maeda, R. Tsuchiya, M. Shinohara, O. Ishiyama, T. Yonezawa, M. Yoshimoto, and H. Koinuma, Science **266**, 1540 (1994).

[39]C. P. Lu, G. Li, J. Mao, L. M. Wang, and E. Y. Andrei, Nano Lett. **14**, 4628 (2014).

SUPPLEMENTARY MATERIAL

Utilizing Complex Oxide Substrates to Control Carrier Concentration in Large-Area Monolayer MoS$_2$ Films

Xudong Zheng,[1] Eli Gerber[2], Jisung Park,[1] Don Werder,[1,3] Orrin Kigner,[1] Eun-Ah Kim[4], Saien Xie,[1,4,5,a)] and Darrell G. Schlom[1,5,6,a)]

[1]*Department of Materials Science and Engineering, Cornell University, Ithaca, New York 14853, USA*

[2]*School of Applied and Engineering Physics, Cornell University, Ithaca, New York 14853, USA*

[3]*Cornell Center for Materials Research, Cornell University, Ithaca, New York 14853, USA*

[4]*Department of Physics, Laboratory of Atomic and Solid State Physics, Cornell University, Ithaca, New York 14853, USA*

[5]*Kavli Institute at Cornell for Nanoscale Science, Ithaca, New York 14853, USA*

[6]*Leibniz-Institut für Kristallzüchtung, Max-Born-Str. 2, 12489 Berlin, Germany*

Contents

Section 1 - Experimental methods

MOCVD growth: The growth of monolayer MoS$_2$ was carried out in a 95 mm (inner diameter) hot-wall quartz tube furnace. Molybdenum hexacarbonyl (Mo(CO)$_6$, MHC, Sigma Aldrich, 99.9% purity) and diethyl sulfide ((C$_2$H$_5$)$_2$S, DES, Sigma Aldrich, 98 % purity) were used as chemical precursors for molybdenum and sulfur. They entered the furnace in the gas phase due to their high equilibrium vapor pressure near room temperature.[1] SAES in-line gas purifiers were used to remove residual water vapor and oxygen from ultra-high purity H$_2$ and Ar. The growth was performed at 600 ℃ with a total pressure of 5.98 Torr. The flow rates were 6 sccm for MHC, 0.3 sccm for DES, 1 sccm for H$_2$, and 1200 sccm for Ar, which were regulated by mass flow controllers (MFC). The growth time for continuous monolayer MoS$_2$ was 2.25 hours on SiO$_2$, 2.5 hours on SrTiO$_3$, 2.8 hours on LaAlO$_3$, and 3.3 hours on MgAl$_2$O$_4$. The growth time can be further reduced to 0.83 hours on SiO$_2$ by increasing the growth pressure and flow rates while still achieving uniformity over large-area substrates (see Figure S6). NaCl was loaded in the upstream region to act as a nucleation suppressant during the growth.[1]

Raman and Photoluminescence Spectroscopy: The Raman and PL spectra were excited with a 532 nm laser under ambient conditions in a confocal Raman spectroscopy system (WItec-Alpha300 R). A 100× objective was used with a numerical aperture of 0.9 and a working distance of 1 mm. The laser power on the sample was 1 mW. Multiple spectroscopy measurements were taken across the substrates. The background signal measured on bare substrates under the same measurement conditions were subtracted for Raman and PL analysis.

MINT calculations: To calculate the charge transfer between MoS$_2$ and the substrates, we use *ab initio* mismatched interface theory (MINT)[2] and perform density-functional theory (DFT) calculations of increasingly large MoS$_2$ clusters consisting of 3-, 6-, 12-, and 18-Mo atoms above a substrate layer. From finite-size scaling of the cluster calculations we predict charge transfer to MoS$_2$ of 3.30, 1.38, 1.15, and 0.97 (in units of 10^{13} cm^{-2}) from SiO$_2$, MAO, LAO, and STO, respectively. The *ab initio* MINT calculations were carried out within the total-energy plane wave density-functional pseudopotential approach, using Perdew-Burke-Ernzerhof generalized gradient approximation functionals[3] and optimized norm-conserving Vanderbilt pseudopotentials.[4] Plane wave basis sets with energy cutoffs of 30 Hartree were used to expand the electronic wave functions. We used fully periodic boundary conditions and a $9 \times 9 \times 1$ k-point mesh to sample the Brillouin zone. Electronic minimizations were carried out using the analytically continued functional approach starting with an LCAO initial guess within the DFT++ formalism,[5] as implemented in the open-source code JDFTx[6] using direct minimization via the conjugate gradients algorithm.[7] All unit cells were constructed to be inversion symmetric

about $z = 0$ with a distance of ≈ 60 Bohr between periodic images of the substrate, using Coulomb truncation to prevent image interaction.

## Section S2 - Raman and PL spectra of MoS₂ on complex oxides compared to bare substrates
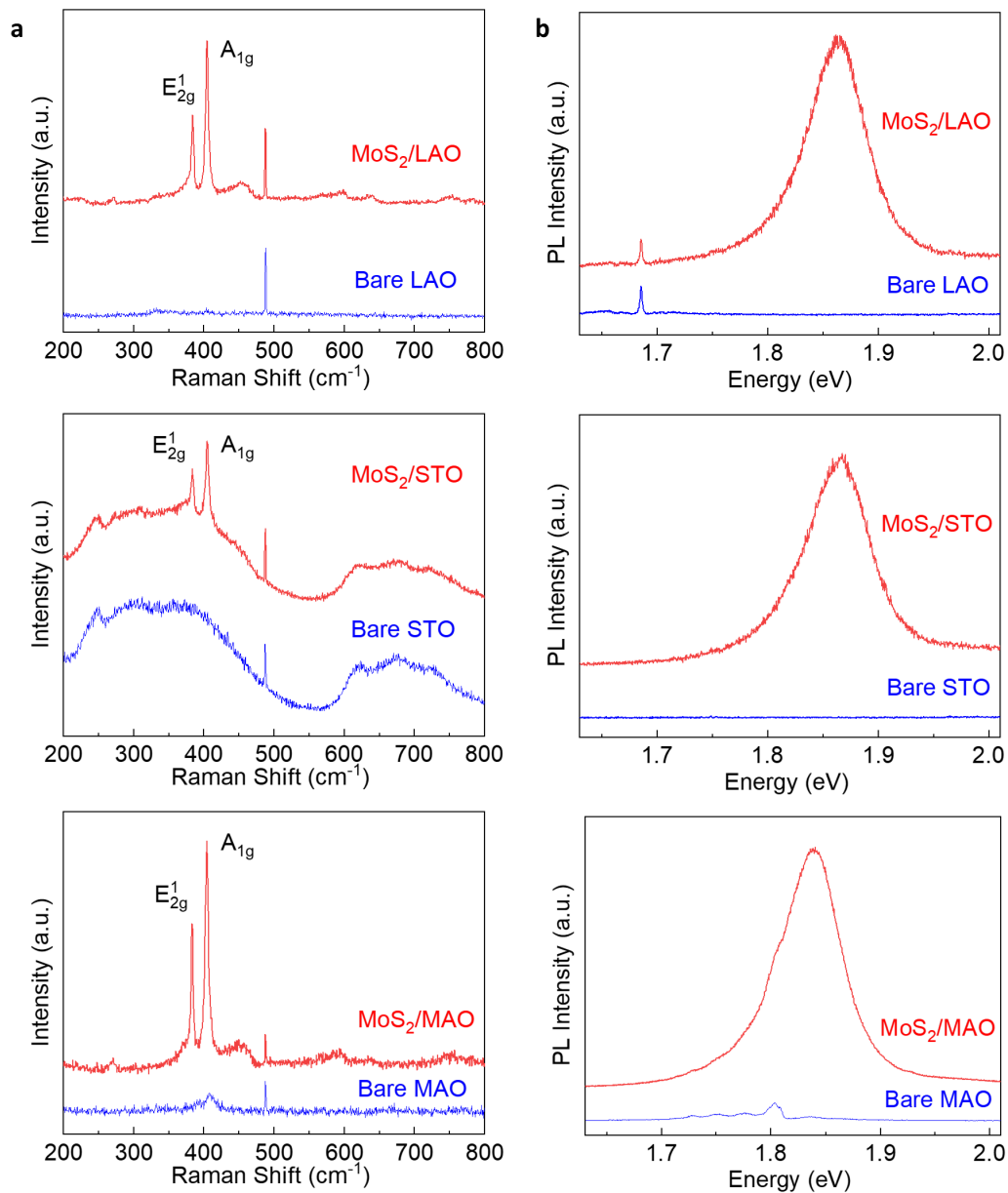
FIG. S1. (a) Raman and (b) photoluminescence spectra of monolayer MoS₂ grown on LaAlO₃, SrTiO₃, and MgAl₂O₄, respectively, with comparison to signals from bare substrates.

# Section S3 - Growth uniformity of MoS₂ on complex oxide substrates
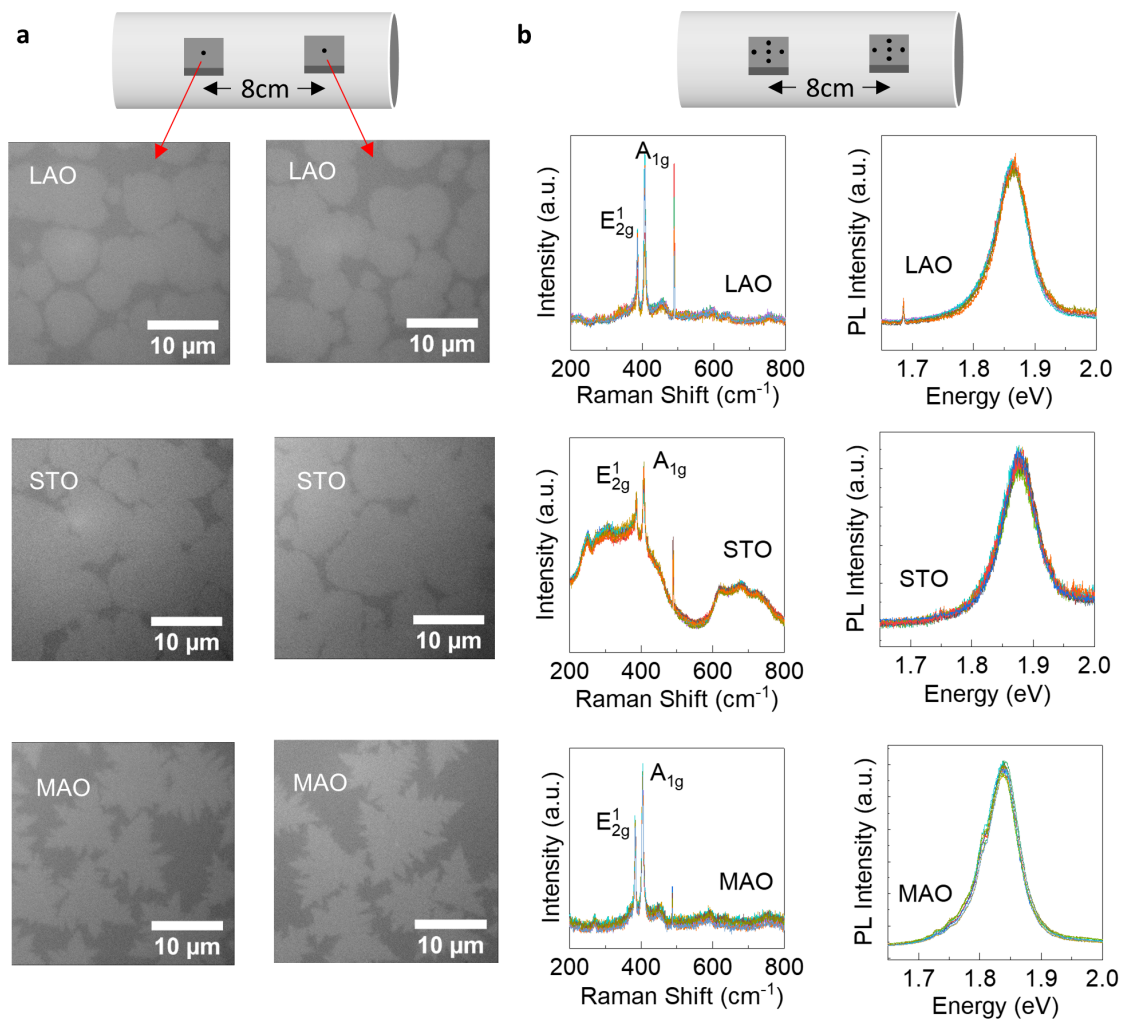
FIG. S2. (a) Optical micrographs of MoS₂ grown on two identical substrates placed 8 cm apart in the MOCVD furnace. (b) Raman and photoluminescence spectra of MoS₂ on complex oxides measured from ten different locations at the positions marked in the schematic diagram.

Section S4 - Optical microscope images of uniform MoS$_2$ growth on a 2-inch SiO$_2$ wafer
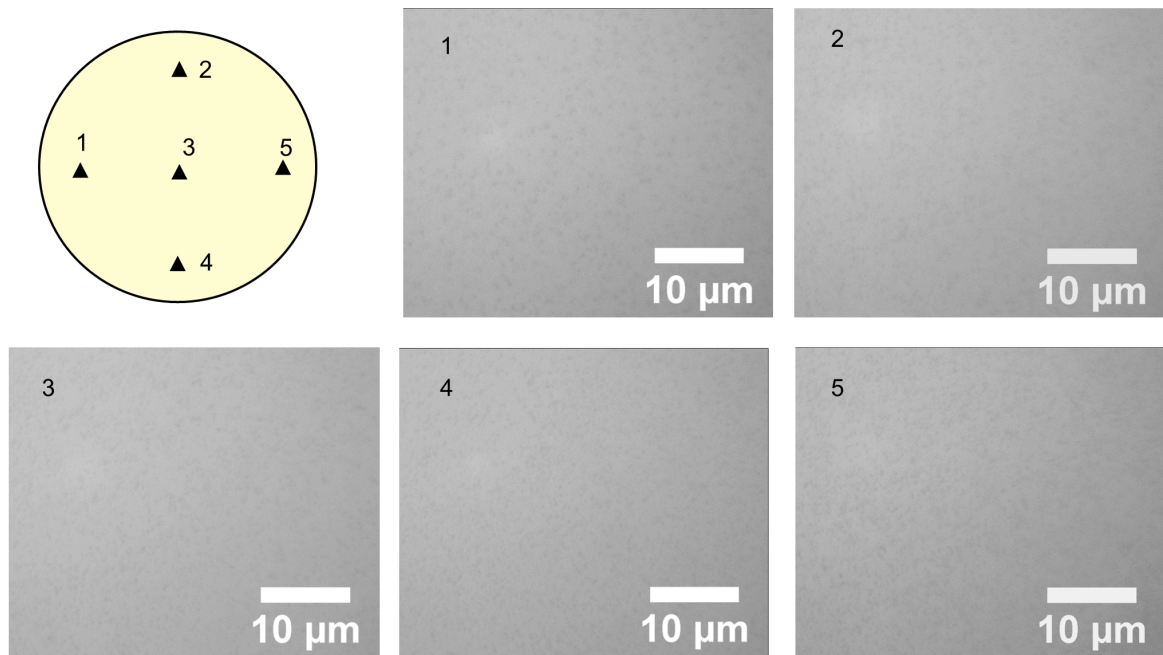
FIG. S3. (a) Optical micrographs of MoS$_2$/SiO$_2$ taken at the locations marked on the schematic of the corresponding wafer.

Section S5 – MINT calculations of electron transfer from oxide substrates to MoS$_2$.
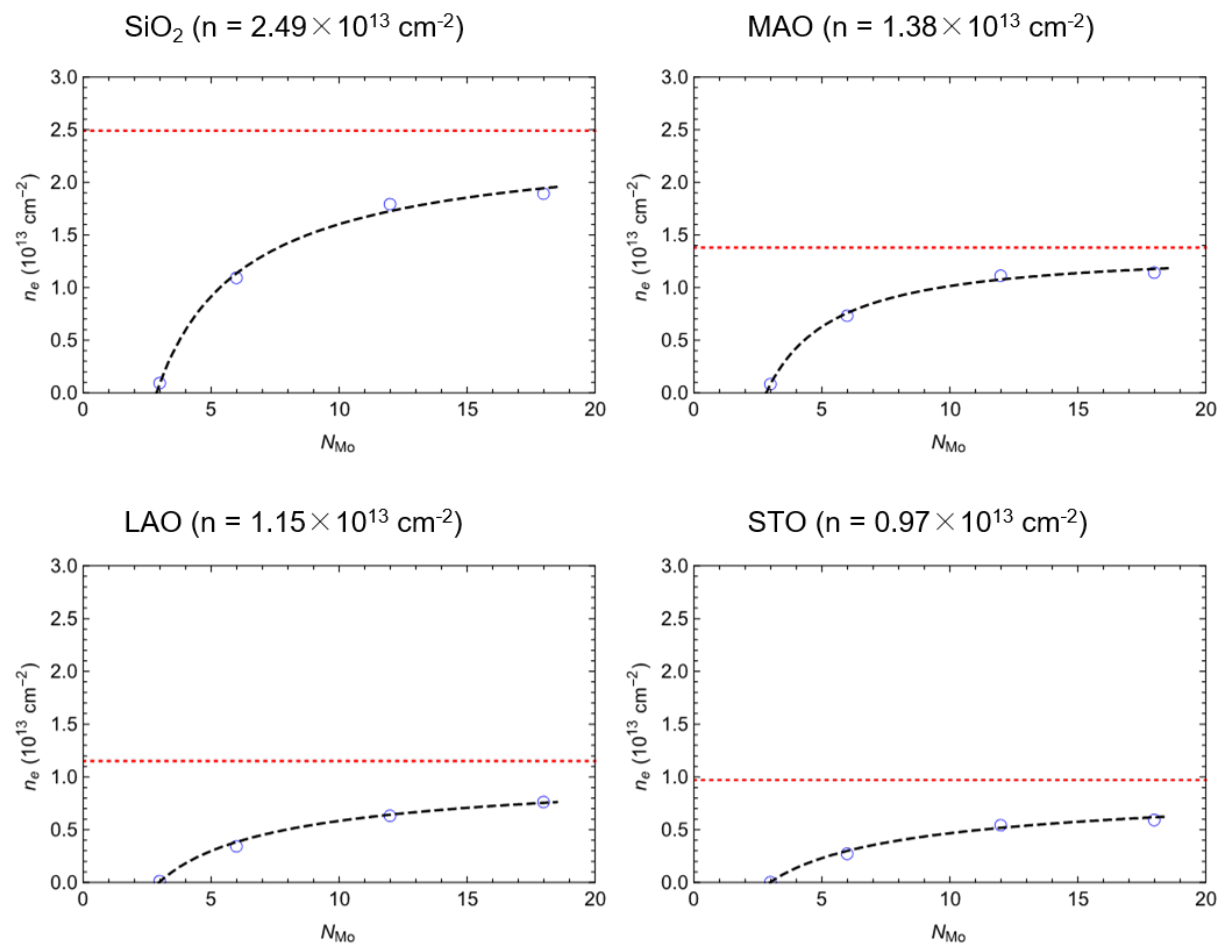
FIG. S4. Convergence of calculated electron doping n$_e$ of MoS$_2$ based on MoS$_2$ cluster-oxide heterostructures with increasing cluster size on (a) SiO$_2$, (b) MgAl$_2$O$_4$, (c) LaAlO$_3$ and (d) SrTiO$_3$. In each plot, the value of electron concentration of MoS$_2$ (marked by the red dashed line) is extrapolated from the power law fitting (black dashed line) of the calculated values for different MoS$_2$ cluster sizes (blue circles).
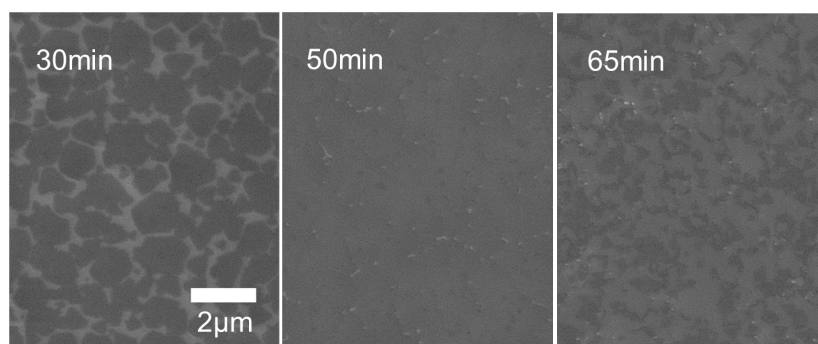
Section S6 - Growth of MoS₂ on other oxide substrates
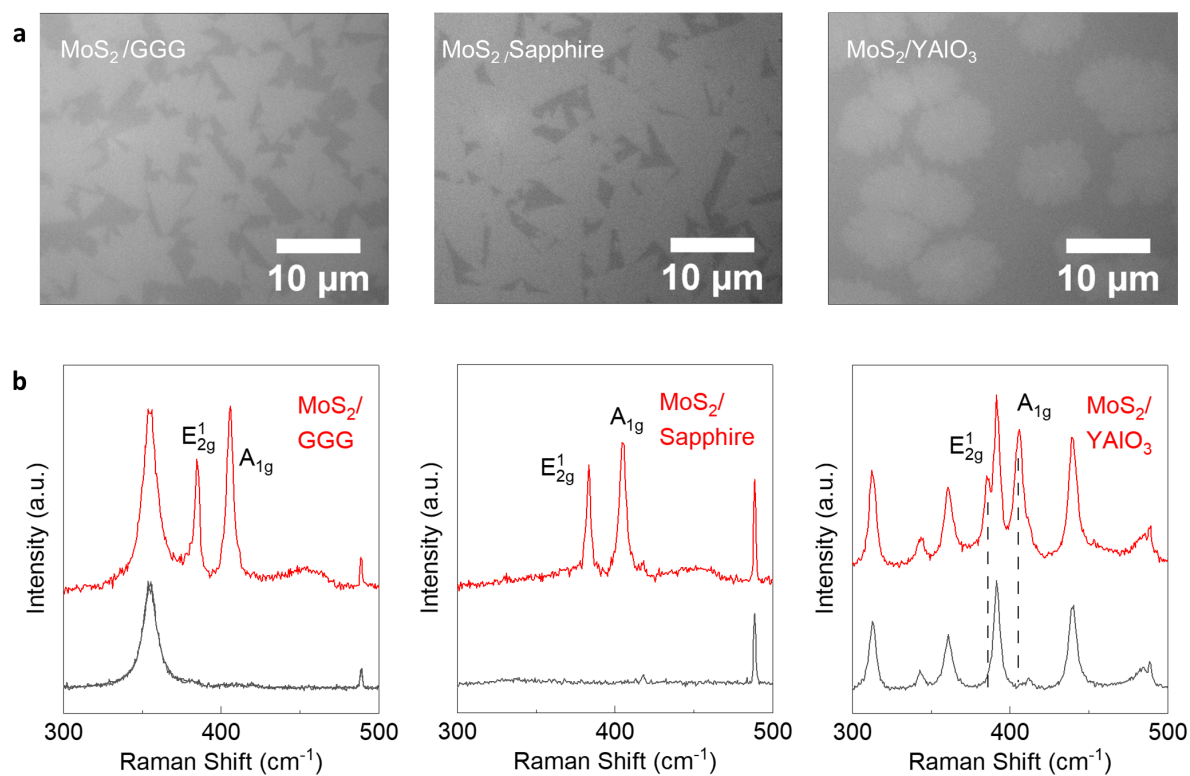
FIG. S5. (a) Optical micrographs and (b) Raman spectra of monolayer MoS₂ grown on GGG, sapphire, and YAlO₃ substrates, respectively.

Section S7 - Fast growth of MoS₂ on SiO₂ substrates

FIG. S6. Scanning electron microscopy (SEM) images of MoS₂ grown on SiO₂ in different growth times. A continuous monolayer is reached at a growth time of 50 min.

Section S8 – Charge transfer between MoS_2 and Nb-doped $SrTiO_3$

We have grown MoS_2 on 0.05 wt.% Nb-doped (100) $SrTiO_3$ (Nb:$SrTiO_3$) and the charge transfer observed in Nb:$SrTiO_3$, which is electron doped that elevate its fermi level,[8] is larger than undoped $SrTiO_3$. This is expected because due to the heavy electron doping, the Fermi level of the Nb:$SrTiO_3$ is set to be very close to the conduction band, far above the charge neutrality level of undoped $SrTiO_3$. Raman spectra [Fig. S6(a)] reveal that MoS_2 grown on Nb:$SrTiO_3$ shows a A_{1g} peak position of 404.9 ± 0.04 cm^{-1}, which is 0.71 ± 0.06 cm^{-1} smaller than that of MoS_2 grown on undoped $SrTiO_3$ [Fig. S6(b)], suggesting a greater electron transfer from Nb:$SrTiO_3$ to MoS_2.
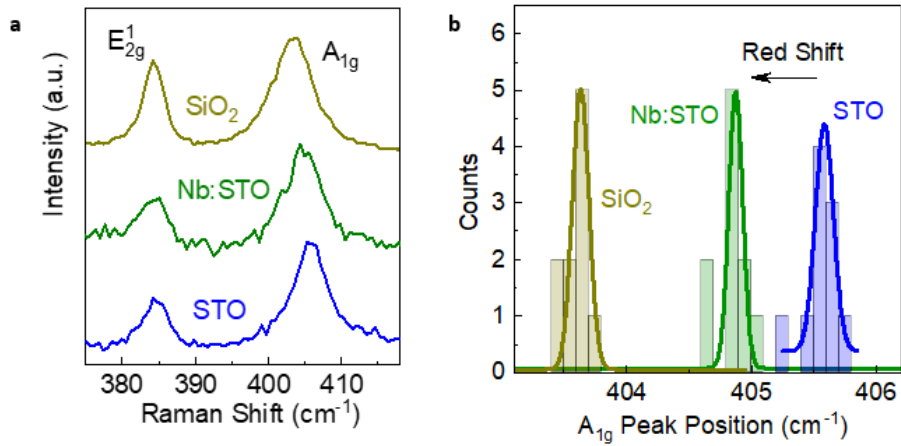

FIG.S7. Raman of monolayer MoS_2 deposited on SiO_2, Nb-doped $SrTiO_3$ and undoped $SrTiO_3$ substrates. (a) Normalized Raman spectra of monolayer MoS_2. (b) Histograms and their Gaussian fittings of A_{1g} peak position of MoS_2 on different substrates.

REFERENCES:

[1]K. Kang, S. Xie, L. Huang, Y. Han, P. Y. Huang, K.F. Mak, C. J. Kim, D. Muller, and J. Park, Nature **520**, 656 (2015).

[2]E. Gerber, Y. Yao, T.A. Arias, and E.A. Kim, Phys. Rev. Lett. **124**, 106804 (2020).

[3]J.P. Perdew, K. Burke, and M. Ernzerhof, Phys. Rev. Lett. **77**, 3865 (1996).

[4]M. Schlipf and F. Gygi, Comput. Phys. Commun. **196**, 36 (2015).

[5]C. Freysoldt, S. Boeck, and J. Neugebauer, Phys. Rev. B **79**, 241103 (2009).

[6]R. Sundararaman, K. Letchworth-Weaver, K. A. Schwarz, D. Gunceler, Y. Ozhabes, and T. Arias, SoftwareX **6**, 278 (2017).

[7]M. C. Payne, M. P. Teter, D. C. Allan, T. A. Arias, and J. D. Joannopoulos, Rev. Mod. Phys. **64**, 1045 (1992).

[8]T. Ma, R. Jacobs, J. Booske, and D. Morgan, APL Mater. **8**, 071110 (2020).